



# Direct 3D printing of a two-part silicone resin to fabricate highly stretchable structures

Saleh Gharai<sup>1</sup> · Ali Zolfagharian<sup>1</sup> · Amir Ali Amiri Moghadam<sup>2</sup> · Nurul Shukur<sup>1</sup> · Mahdi Bodaghi<sup>3</sup> · Bobak Mosadegh<sup>4</sup> · Abbas Kouzani<sup>1</sup>

Received: 23 October 2022 / Accepted: 19 February 2023 / Published online: 16 March 2023  
© The Author(s) 2023

## Abstract

The direct ink writing (DIW) method of 3D-printing liquid resins has shown promising results in various applications such as flexible electronics, medical devices, and soft robots. A cost-effective extrusion system for a two-part high-viscous resin is developed in this article to fabricate soft and immensely stretchable structures. A static mixer capable of evenly mixing two viscous resins in an extremely low flow regime is designed based on the required mixing performance through a series of biphasic computational fluid dynamics analyses. The printing parameters of the extrusion system are determined empirically, and the mechanical properties of the printed samples are compared to their molded counterparts. Furthermore, some potential applications of the system in soft robotics and medical training are demonstrated. This research provides a clear guide for utilizing DIW to 3D print highly stretchable structures.

**Keywords** 3D printing of silicone · 3D printing · Static mixer · Biomedical · Soft robotic

## List of symbols

$A$	Cross-sectional area of the nozzle tip
$B$	Die-swelling ratio
$\bar{c}$	Mean concentration
$c_i$	Concentration at point $i$
$D$	Nozzle diameter
$D_E$	Extruded ink diameter
$\underline{D}_s$	Strand diameter
$F$	Body force
$g$	Gravitational constant
$H$	Layer height
$\dot{m}$	Mass flow rate
$\dot{m}_{pq}$	Mass transfer rate from phase $p$ to $q$

$\dot{m}_{qp}$	Mass transfer rate from phase $q$ to $p$
$N$	Power law index
$N$	Number of sample points
$n_i$	Index for previous time step
$P$	Pressure
$R$	Radius in an orthogonal direction
$V$	Print speed
$\underline{W}$	Layer width
$V_q$	Mass average velocity of phase $q$
$V_0$	Extrusion velocity
$Q$	Volume flow rate
$\alpha_q$	Volume fraction
$\dot{\gamma}$	Shear rate

✉ Saleh Gharai  
gsaleh@deakin.edu.au

Ali Zolfagharian  
a.zolfagharian@deakin.edu.au

Amir Ali Amiri Moghadam  
aamirimo@kennesaw.edu

Nurul Shukur  
n.mohdshukur@deakin.edu.au

Mahdi Bodaghi  
mahdi.bodaghi@ntu.ac.uk

Bobak Mosadegh  
bom2008@med.cornell.edu

Abbas Kouzani  
abbas.kouzani@deakin.edu.au

- <sup>1</sup> School of Engineering, Deakin University, Geelong, VIC 3216, Australia
- <sup>2</sup> Department of Robotics and Mechatronics Engineering, Kennesaw State University, Marietta, GA 30060, USA
- <sup>3</sup> Department of Engineering, School of Science and Technology, Nottingham Trent University, Nottingham NG11 8NS, UK
- <sup>4</sup> Dalio Institute of Cardiovascular Imaging, Department of Radiology, Weill Cornell Medicine, New York, NY 10021, USA

$\Delta p$	Pressure drop
$\mu$	Viscosity
$\rho$	Density
$\rho_q$	Density of phase q
$\sigma$	Surface tension coefficient

## 1 Introduction

Liquid silicone resins (LSRs) are thermoset materials that are viscous liquids in their initial uncured state and solid after being polymerized by mixing their oligomer and catalytic parts. LSRs have been used in a variety of applications in the medical field [1, 2], soft robotics [3, 4], and advanced electronics [5] domains. Conventional techniques for the fabrication of silicone structures such as molding [6] and soft lithography [7] are costly and time-consuming processes and have several limitations, including the inability to perform rapid and precise fabrication of highly complex structures, and structures with internal voids. Direct additive manufacturing (AM) of LSRs can address the limitations of conventional methods, enabling the fabrication of intricate designs [8]. Since the early 2010s, various methods (e.g., material extrusion, material jetting, freeform reversible embedding (FRE), and vat photopolymerization (VPP)) have been investigated to directly 3D print silicone; multiple literature reviews discuss their processes and applications in detail, elsewhere [9, 10]. In the VPP method, an ultraviolet (UV) light is deployed to fabricate a model, layer-by-layer, in a vat of photopolymer resin. The first application of the VPP method to 3D print silicone was shown by Femmer et al. [11]. They used a commercial digital light processing (DLP) system for printing Polydimethylsiloxane (PDMS) membranes and obtained a lateral resolution of 150  $\mu\text{m}$ . Other VPP systems such as the stereolithography (SLA) [12] and low one-photon polymerization (LOPP) [13] have been explored to print silicone. Bhattacharjee et al. [12] printed small PDMS models with a resolution of  $\sim 50 \mu\text{m}$  which is significantly superior compared to the reported resolution of 1–2 mm using the LOPP technique [13]. Overall, however, 3D-printed structures using VPP systems have a limited stretchability property (i.e.,  $< 250\%$  elongation at break) [9, 12–14]. Recent advances in the development of UV/thermal curing silicones [15] demonstrated the possibility of utilizing a dual curing UV/thermal system to fabricate silicone structures with high stretchability (elongation at break  $\sim 1400\%$ ). However, the separation of the printed layers due to the strong adhesion of a cured silicone to the surface of a vat is still one of the main obstacles to using SLA and DLP techniques for 3D printing silicone [16].

Material jetting or inkjet printing utilizes the deposition of fluid droplets which are solidified by solvent evaporation or photo-curing. Conventional jetting systems are only compatible with low-viscosity fluids and are not capable of depositing high-viscous fluids such as silicone [17]. McCoul et al. demonstrated the possibility of printing very fine silicone membranes with a resolution of 2–4  $\mu\text{m}$  [18]. However, this system was incompatible with highly viscous ink limiting its capability to 3D print highly stretchable structures. The new generation of jetting printheads can print highly viscous inks up to  $10^6 \text{ mPa}\cdot\text{s}$ . Dual systems such as UV-extrusion Ink jetting [19] and piezoelectric-pneumatic [20, 21] systems demonstrated the possibility of fabricating silicone structures at a velocity of 100 mm/s with a resolution of 500–600  $\mu\text{m}$ . Nevertheless, preparing the required ink is extremely challenging [22], and 3D printing of a large and complex structure made of silicone using the dual systems has not been demonstrated yet.

W. Feinberg et al. [23] fabricated helical tubes from a PDMS material using the FRE method. In this method, a PDMS ink was prepared by mixing Sylgard 184 (Dow Corning) in a 10:1 base-to-curing agent ratio and deposited layer by layer in a vat of polyacrylic acid (PAA) gel. The printing was freeform as no auxiliary structural support was used; only the PAA gel provided support to the PDMS during its polymerization, which occurred over 4 h at 65  $^\circ\text{C}$  or 72 h at 20  $^\circ\text{C}$ . The embedded PDMS print was then released by a phosphate buffer solution. This method enabled the printing of a wide range of hydrophobic materials such as cycloaliphatic epoxies and fluoroelastomers on hydrophilic support with a resolution ranging from 140 to 400  $\mu\text{m}$ . O'Bryan et al. [24] improved the resolution of the silicone parts to 30  $\mu\text{m}$  by replacing the PAA gel with an oil-based micro-organogel support material, although the support materials used in the FRE technique are inexpensive and can provide a stable printing environment over a long period. However, in this method, the lateral pressure between the printed layers is largely diminished as printed layers are suspended in the supporting gel. This issue may hinder lateral fusion and the mechanical integrity of the printed parts. Furthermore, the printing path must be optimized to avoid trapping the support within the voids inside the printed objects.

Compared to other AM methods, material extrusion systems can deposit a broader range of fluids with viscosity ranging from  $\sim 30$  up to  $6 \times 10^7 \text{ mPa}\cdot\text{s}$  [25–28]. The capability of extruding high-viscous materials makes this process suitable for printing silicone as high-viscous polymers ( $\mu > 10^4 \text{ mPa}\cdot\text{s}$ ) have better shape retention. Importantly, highly viscous silicones are more stretchable due to their longer polymer chains [10]. However, 3D printing of silicone elastomers without supporting materials or the direct ink writing (DIW) method is quite challenging as the viscosity

of a silicone mixture should be low enough to be extruded from the printing nozzle, while simultaneously being large enough to resist wetting out, such that it can retain its shape before curing [29, 30]. Various techniques [31–33] have been used to circumvent the supporting gel by altering the viscosity of silicone and accelerating the cure time by means of added catalysts, heat, or a combination of both. Morrow et al. [31] used a combination of thickening additive and heat for the direct printing of silicone elastomers. Specifically, the two-part EcoFlex 00-30 (Smooth-On, Macungie, PA, USA) platinum cure silicone mixture was premixed with a urefil-11 additive upon extrusion to improve the shape retention while a heat gun accelerated the curing time. This early study demonstrated that silicon could be printed directly without any supporting material. However, this method was a tedious process as the printing had to be paused every 10–15 s between each printed layer to manually elevate the processing temperature by the heat gun. In addition, the printing time was limited to 15 min as the silicone crosslinking inside the syringe would alter the properties of the silicone enough to disrupt the printing performance. The abrupt printing process led to poor quality and large discrepancies between the actual and printed geometries. This process can be improved by designing a printing nozzle to mix the polymer and crosslinker homogeneously upon extrusion. Yirmibesoglu et al. [32] developed an active mixer that consists of a mixing chamber with two inlets and a spinning paddle operated by a servo motor. Polymer and crosslinker of Dragon skin 10 (Smooth-On, Macungie, PA, USA) were injected into the mixing chamber by a syringe pump and mixed homogeneously by the paddle rotating at 100 RPM. Similar to the previous study, a thickening additive was used to improve the shape fidelity in the elevated printing temperature by convective heating. It is shown that the extrusion machine is capable of 3D printing somewhat complex structures with 5 to 17% dimensional errors. The volumetric printing speed was 0.3 mL/min, translating to ~3 h of printing time for an 8-channel bending actuator. Since Dragon skin (Smooth-On, Macungie, PA, USA) is a very fast platinum cure system with a short pot life of  $\approx 4$  min and a cure time of ~30 min, the residual of the mixture in the nozzle would cause clotting in the mixing chamber, disrupting the printing performance. Furthermore, the active mixer had five components requiring precise fabrication and leak-free assembly, along with an additional power source and control system to be integrated with the printing process. Considering the fact that the mixer needs to be replaced after each printing run, and the difficulty associated with manufacturing and integration of such a mixer, incorporating an active mixer is highly impractical compared to a static mixer. However, the flow regime (i.e., 0.3 mL/min) in DIW is too slow to provide adequate pressure energy, as required for mixing in static mixers. Hence, such a mixer should have adequate flow-restriction features

(i.e., smaller flow channels or extended channel length) to generate the required pressure drop, which proportionally increases the force needed to pump resins. The substantially greater pumping force required by static mixers could be fulfilled by incorporating a high-torque syringe pump or multiple pumps [33]. Miriyev et al. [33] developed a static mixer used in a multi-extrusion system for the direct printing of silicone. In this study, *Part A* and *Part B* of EcoFlex 00-35 (Smooth-On, Macungie, PA, USA) polymer were injected into a static mixer upon extrusion. Although it is shown that the static mixer could homogeneously mix the polymer and crosslinker, a multi-pump system with individual servo motors was required to push the resins through the mixer.

The disrupted printing process, particular requirements for manufacturing and integration of an active mixer, and substantial pumping force in using a static mixer are major barriers to the DIW of silicone elastomers. In addition, the maximum viscosity of resins in the previous studies was ~23000 mPa.s [32], and a system capable of printing more viscous resins translating to the higher stretchability of the printed structures has yet to be developed.

In this study, we aimed to develop a cost-effective extrusion system capable of direct 3D printing of a highly viscous resin to fabricate stretchable structures, all while providing a minimally disturbed printing process and avoiding the need of using multiple pumps or an active mixer. A static mixer is developed through a series of CFD analyses to evenly mix high-viscous resins in an extremely low flow regime without necessitating a significant pumping force. The printing parameters were determined empirically, and the applications of the extrusion system are shown for both soft robotic and medical training.

## 2 Methodology

### 2.1 Static mixer design

Kenics static mixer (KSM) is one of the most common commercial mixers with the application of mixing high-viscous fluids. The KSM and two novel static mixers were constructed as shown in Fig. 1. The KSM is usually composed of helical blades with a twist angle of  $180^\circ$  arranged in a series of left- and right-handed twists. In this study, the diameter of the KSM is 12 mm and contains 4 mixing elements. The length of the mixers was kept constant at 80 mm. The first novel mixer is designed with three mixing elements, each element consists of a funnel-shaped channel and  $180^\circ$  twisted helical blades as illustrated in Fig. 1b. The twist angle is increased to  $360^\circ$  for the second novel mixer as presented in Fig. 1c.

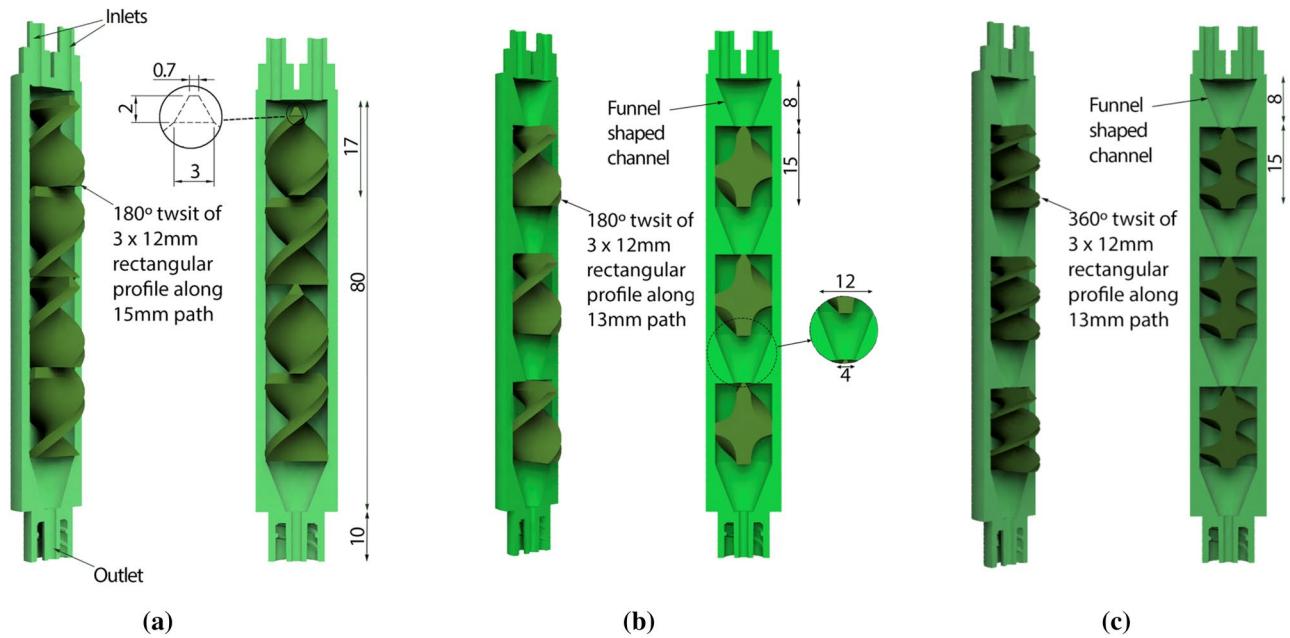


**Fig. 1** 3D CAD rendering of mixers. **a** Kenics static mixer, **b** Novel Design-1 Mixer (ND1M), **c** Novel Design-2 Mixer (ND2M). All dimensions are in mm

## 2.2 CFD modeling of the static mixers

The multiphase Volume of Fluid (VoF) simulations were performed using ANSYS Fluent (version 2021 R2) for tracking EcoFlex 00-50 (*Part A–Part B*) dispersion in the static mixers. The solver was a pressure-based type with PISCO scheme for pressure–velocity coupling. The 3D domains were discretized by tetrahedron elements. The Courant number was kept below 1, giving a time step of  $10^{-4}$ . The convection terms were discretized with a second-order upwind scheme, and the least squares cell-based gradient calculation scheme was used for the temporal discretization of pressure gradient computations. The continuity equation (Eq. 1) [34] was solved to separate the phases by tracking the interface for the volume fraction of the phases:

$$\frac{1}{\rho_q} \left[ \frac{\partial}{\partial t} (\alpha_q \rho_q) + \nabla \cdot (\alpha_q \rho_q \vec{V}_q) \right] = \sum_{p=1}^{n_i} (\dot{m}_{pq} - \dot{m}_{qp}) \quad (1)$$

The momentum Eq. (2) is solved throughout the domain, and the resulting velocity field is shared among the phases:

$$\frac{\partial}{\partial t} (\rho \vec{V}) + \nabla \cdot (\rho \vec{V} \vec{V}) = -\nabla_p + \nabla \cdot \left[ \mu \left( \nabla \vec{V} + \nabla \vec{V}^T \right) \right] + \rho \vec{g} + \vec{F} \quad (2)$$

The above equation is dependent on the VoFs of all phases through the properties of  $\rho$  and  $\mu$ . The continuum surface force (CSF) model is used to model surface tension. The CSF model

incorporates surface tension into the VoF calculation, resulting in a source term for the momentum Eq. (2). The  $\sigma$  is calculated from (Eq. 3) by computing the  $\Delta p$  across the surface:

$$p_2 - p_1 = \sigma \left( \frac{1}{R_1} + \frac{1}{R_2} \right) \quad (3)$$

A homogenous mixture should have even distributions of species. Hence, the homogeneity level is determined by measuring concentration distributions. Coefficient of Variation (CoV) is a widely used measure for evaluating the uniformity of concentration at a cross-section of static mixers [35]. The homogeneity of the mixture was quantified using Eq. (4) to evaluate the mixing performance of the mixers:

$$CoV = \frac{\sqrt{\frac{1}{n-1} \sum_{i=1}^n (c_i - \bar{c})^2}}{\bar{c}} \quad (4)$$

### 2.2.1 Boundary conditions

The boundary conditions for the inlets are set to be 0.3 mL/min for both *Part A* and *Part B* to match the parameters of the experimental study and zero-gauge pressure is applied at the outlet. The no-slip boundary condition is utilized on the tube wall and element surfaces. The Reynolds number for a flow rate of 0.3 mL/min was calculated as  $3.87 \times 10^{-5}$  at the inlets. The flow was assumed laminar and modeled for a

**Table 1** Liquid properties of EcoFlex 00-50 polymer with 4% v/v of THIVEX at 21.4 °C

Properties	EcoFlex 00-50
Density, $\rho$ [kg/m <sup>3</sup> ]	1070
Viscosity, $\mu$ [mPa.s]	81,881
Interfacial Tension [mN/m]	18.9 [39]

period of 20 s in all cases. The convergence criteria were set to be  $10^{-5}$ . The material properties are defined according to the values listed in Table 1. The viscosity of uncured silicone is stable and varies insignificantly due to the increased temperature by the heater [36]. Moreover, the heater element is only needed to avoid the self-collapsing of parts taller than  $\approx 20$  mm. Thus, the added heat by a heater was not considered in this study to simplify the CFD simulation.

**2.2.2 Model validation and mesh independency test**

CFD results are more sensitive to calculated pressure than velocity as pressure gradients determine the flow characteristics. Hence, to assess the validity of the CFD results, the predicted  $\Delta p$  across the KSM mixer was compared with the experimental data. The KSM mixer is 3D printed by an SLA printer (Anycubic, Photon Mono X 6 K). The modified EcoFlex 00-50 was injected into the mixer at a flow rate of 0.3 mL/min. The upstream and downstream pressures were measured just proximal to the first mixing element and just distal to the last element. The mesh size was refined until the predicted  $\Delta p$  was in good agreement with the experimental data and  $\Delta p$  was independent to further refinement of the grid size.

**2.3 Printing system**

The static mixer was attached to a printer head as shown in Fig. 2. A dual syringe pump (NE-4000X, Adelab Scientific, Australia) was used to inject the modified EcoFlex 00-50 Part A and Part B resins into a static mixer through 5 mm tubes. A 150 W ceramic heater was used to further accelerate the curing time. The cost of assembling the printing system is listed in Table 2.

**2.4 Optimization of printing parameters**

The printing parameters were determined empirically by analyzing the printed mono-fibers. Figure 3 shows the printing parameters for the DIW process. It is well established that the extruded strand diameter  $D_s$  is different from the extruded ink diameter  $D_e$  due to the viscoelasticity characteristic of the ink. The theoretical value of  $D_s$  can be calculated based on the conservation of volume using Eq. (5). A nozzle with an ID of 0.81 mm at its tip and a print height of 1 mm was used as the

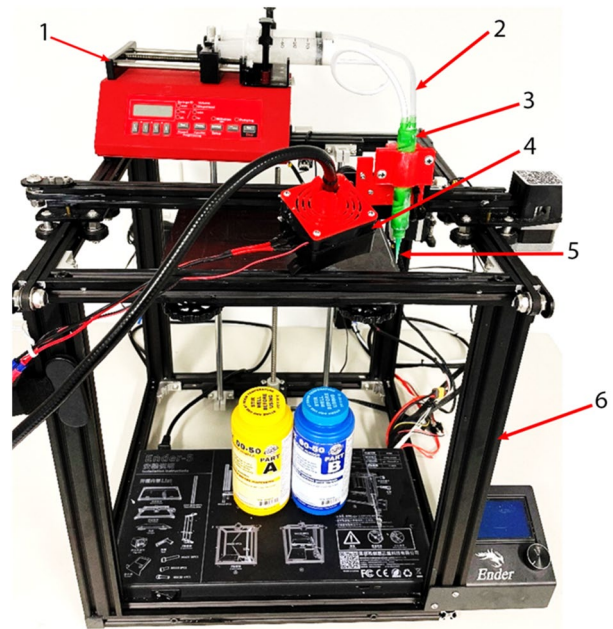


**Fig. 2** The 3D printing system. 1) New Era Dual NE-4000X syringe pump (Adelab Scientific, Australia) with two 50 mL syringes, 2) a 5 mm ID vinyl tube, 3) a 3D-printed ND2M mixer, 4) a generic 24 V 150 W ceramic heater, 5) 18-gauge luer-lock nozzle, 6) Ender 5 pro gantry system

**Table 2** The approximate cost of the printing system

Item	Cost (AUD)
Dual syringe pump	\$1600
Ender Pro 3 V2 printer	\$300
Ceramic heater	\$36
Static mixer	$\approx$ \$2
18-gauge tapered dispensing tip	$\approx$ \$1

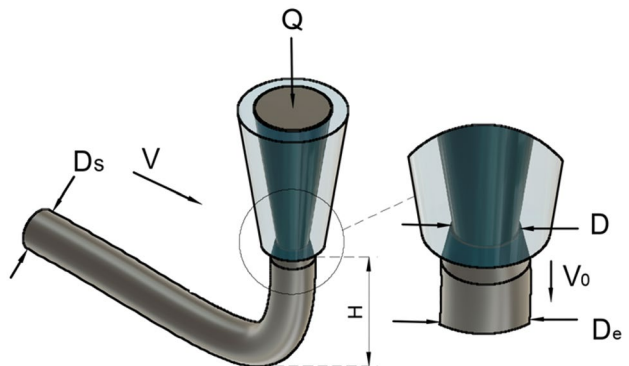


**Fig. 3** The typical 3D printing parameters for DIW method

basis for the printing experiments. The  $V_0$ , for a given  $A$ , was calculated for a different  $Q$  from Eq. (6):

$$D_s = BD/\sqrt{(V/V_0)} \quad (5)$$

$$V_0 = Q/A \quad (6)$$

The die-swelling ratio  $B$  is a complex rheological phenomenon, and it is related to several factors such as material properties, shear rate, and nozzle tip diameters [37]. However, in our experiments, the rate of change for  $B$  between different printing experiments is assumed to be negligible as the flow regime is extremely low. Hence, the main printing parameters affecting  $D_s$  were identified as  $V$  and  $Q$ . In total, nine combinations of  $V$  (5 mm/s, 10 mm/s, 15 mm/s) and  $Q$  (0.1 mL/min, 0.3 mL/min, 0.5 mL/min) were defined for analyzing the samples. A set of five mono-fibers with 200 mm length was printed for each combination of  $V$  and  $Q$ . The diameter of strand  $D_s$ , was measured by a microscope (Olympus sZ61 TR) in the middle of each printed mono-fiber. The average of taken measurements for the five samples was used to evaluate the print quality.

## 2.5 Materials preparation

### 2.5.1 Silicone elastomer

EcoFlex 00-50 (Smooth-On, Macungie, PA, USA) was selected due to its prevalence as a material for soft and stretchable structures. Furthermore, in comparison to EcoFlex 00-10 and EcoFlex 00-30, its viscosity is greater. Polymers with higher viscosity can be stretched further because their polymer chains are longer. THIVEX™ (Smooth-On, Macungie, PA, USA) was used as a thickening agent. The additive percentage was determined empirically. The two-part silicone polymers were mixed in a 1:1 ratio and the thickening agent was added as a percentage of the total mixing volume. 0.2 mL of silicone/additive mixture was extruded with varying thickener percentages from a syringe with an 18-gauge syringe onto a laminated surface with concentric circles of incrementing 1 mm radii. The 4% v/v sample showed the lowest amount of spread and better feature fidelity. The viscosities of *Part A* and *Part B*, with 4% v/v of thickener, were measured by a viscometer (Model DH-DJ-9 T, Guangdong Hongtuo Instrument Technology). The DIW procedure relies heavily on the polymer's thixotropy. A self-supporting viscosity is necessary for extruded polymers, but a viscosity that is too high might make the extrusion process challenging. Silicone elastomers are suitable candidates for DIW due to their shear-thinning property [8]. The molecular chains

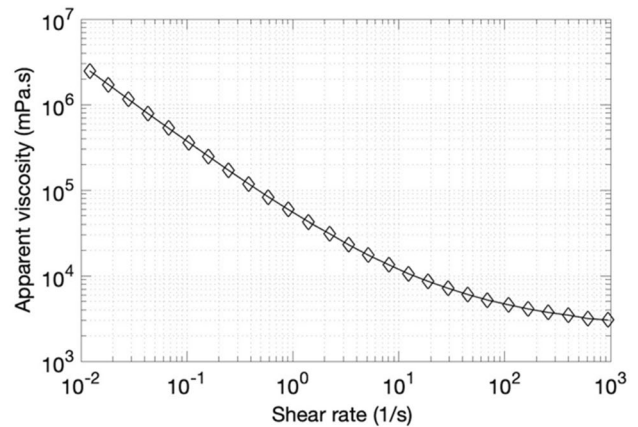


Fig. 4 Shear-thinning plot of EcoFlex-50 silicone

inside the silicone elastomer are entangled with each other and have a high viscosity at low flow rates when the material is at rest, but as the flow rate rises, the molecular chains align in the direction of the shear force, causing the viscosity to decrease [8]. This property of silicone elastomers ensures smooth extrusion and self-supporting molding. The rheological property of EcoFlex 00-50, as shown in Fig. 4, is confirmed to be shear-thinning, which is a necessary for the DIW method [38].

### 2.5.2 Poly (acrylic acid) support bath

The support material was prepared by adding a carbomer 940 to distilled water and then neutralizing the mixture by adding sodium hydroxide until a clear gel (at a PH of 7) was formed. The viscosity of the gel was measured by the viscometer. Various samples were prepared with different w/v % of carbomer 940 to distilled water ranging from 0.25 to 1% to match the viscosity of the gel to EcoFlex 00-50 with 4% v/v of THIVEX. A ring with a diameter of 50 mm was printed in different gel baths using the optimized static mixer to evaluate the effects of various viscosities of the gel baths on the print quality.

## 2.6 Mechanical characterizations of 3D-printed and molded specimens

ASTM D638 IV standard is considered suitable for testing soft silicone rubbers [40]. The mold was designed according to ASTM D638 IV [41]. A set of five molds were made of Poly(lactic acid) (PLA) using a 3D printer (Flashforge-Creator 3 Pro). EcoFlex 00-50 were prepared as described in 2.5.1 and poured into the molds. The molds were put into a vacuum chamber for degassing and visible bubbles were burst manually. The samples were detached from the molds

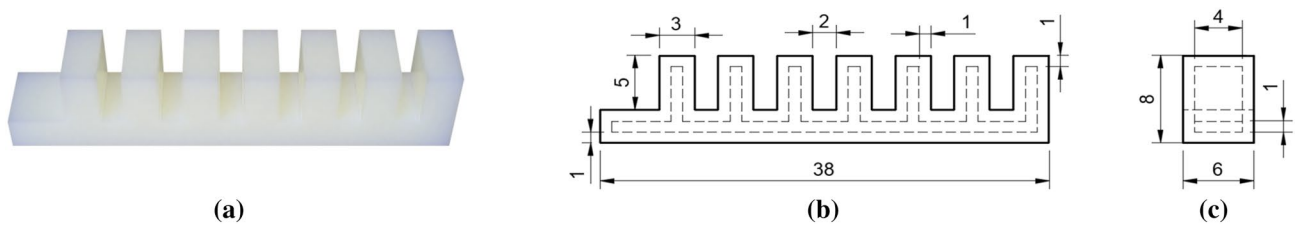


**Fig. 5** CAD model of the pneumatic actuator. **a** 3D CAD rendering of the soft actuator, **b** schematic front view, **c** schematic side view. All dimensions are in mm

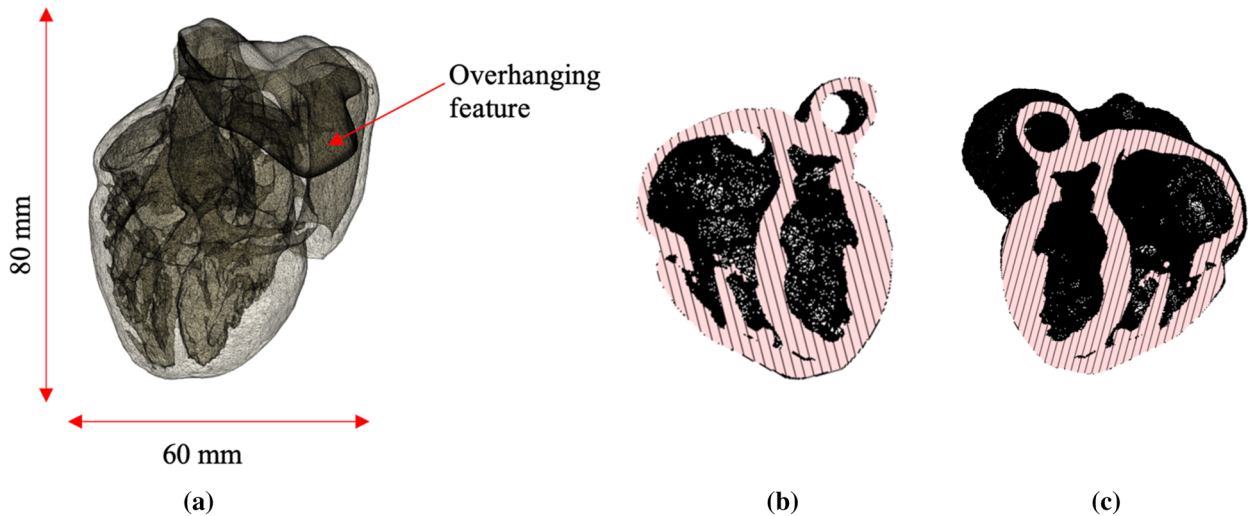


**Fig. 6** CAD model of the heart. **a** Isometric view showing the overall dimensions and the overhanging feature, **b** top view of a cross-section, **c** bottom view of a cross-section

after 4 h for testing. The CAD model of a dogbone specimen is designed in Fusion 360 software based on ASTM D638 IV dimensions and exported as a.stl file into a slicer software. The G-code for the printer is generated to print five samples with the following parameters: *H*: 1 mm, *W*: 1 mm, *V*: 10 mm/s, infill: 100%, and infill pattern: 45° lines. Both molded and 3D-printed samples were tested at a rate of 500 mm/min according to the standard of ASTM [42] using the Instron testing machine (Instron, Norwood, MA, USA.) with a 10 kN load cell.

**2.7 CAD models of the actuator and human heart**

The soft bending actuator is one of the most frequently used actuators in soft robotics. Thus, a bending actuator was designed to demonstrate the capability of the printer for fabricating such an actuator. The actuator is composed of seven

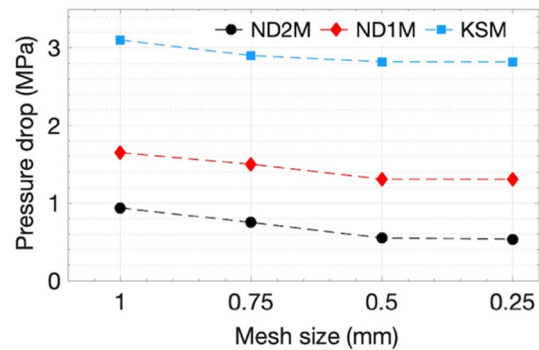


**Fig. 7** CFD mesh convergence study using the pressure drop

chambers with a body thickness of 6 mm, an inner spacing between the chambers of 2 mm, and a length of 38 mm as shown in Fig. 5.

A generic human heart model was retrieved from an online database and scaled down to a manageable size. The detail of other biological models suitable for 3D printing silicone via FRE can be found elsewhere [43]. An overhanging body was manually added to the heart model for evaluating the printing

capability of such a design feature. The heart model shown in Fig. 6 was printed in a gel bath with an optimum % of w/v carbomer/water.

### 3 Results

#### 3.1 Numerical results

##### 3.1.1 Validation and mesh independence study

The  $\Delta p$  was computed for all three mixers with different mesh sizes. It was clear that the predicted  $\Delta p$  from the simulation with 0.5 mm grid size was independent to further mesh refinement for all cases as depicted in Fig. 7. The  $\Delta p = 0.58\text{MPa}$  was measured for KSM as the absolute difference between the inlet and outlet. The CFD simulation underestimated the  $\Delta p (= 0.55\text{MPa})$  by 5%, which is considered to be in good agreement with the experimental data. Accordingly, the current CFD model was deemed suitable for studying the other static mixers.

##### 3.1.2 CFD analysis of the static mixers

A homogeneous network structure is required to achieve an ideal polymer network [44]. By utilizing the numerical technique described in the previous sections, the network homogeneity was evaluated by analyzing the phasic distributions of the two-part polymer across the three mixers. Eco-Flex 00-50 is a two-component liquid silicone with a mix

ratio of 1 to 1. Hence, in the controlled volume mixture, a homogenous network is achieved once i) each component occupies only 50% of the volume ( $\text{VF} = 0.5$ ), and ii) the concentration distribution is uniform. The occupied volume by the components was tracked to evaluate concentration distributions in the mixture. The CFD results plotted VF of *Part B* in Figs. 8, 9, and 10 where the red regions represent a VF of 1 (i.e., 100% of the volume was occupied by *Part B*), and the dark blue regions represent a  $\text{VF} = 0$  (i.e., 0% of the volume was occupied by *Part B*). The variation of VF values for *Part B* was captured by color contours on both the axial and cross-sectional planes of the mixers. The concentration distribution at different sections of the KSM is shown in Fig. 8. The axial contour (Fig. 8a) shows the mixing process across the mixer. *Part A* and *Part B* entered the first element and split into two streams along the surface of that element. *Part B* VF is  $\approx 0.5$  at the interface of two phases before the first element (Fig. 8c) showing the dispersion of the two parts and the formation of the boundary layers separating the two phases. Each element split the stream into two and forced the two phases to collide and rotate along the helical blades. Both streams entered into the next element twisted at  $90^\circ$  with respect to the previous element. The  $90^\circ$  twist splits the stream in a different direction after each element, prompting the dispersive mixing process. The homogenous regions progressively became larger after the third element (Fig. 8f). The central portion of the polymer at the outlet was homogenous, however, the residuals of *Part A* (dark blue region) and *Part B* (red region) remained at the ridge of the outlet (see Fig. 8h). This finding is aligned with our

**Fig. 8** VoF modeling of *Part B* resin in KSM. **a** Axial view at the center, **b** isometric view with cross-sectional views before and after each mixing element, **c–g** zoomed-in cross-sectional views for each shown in **b**, **h** at the outlet

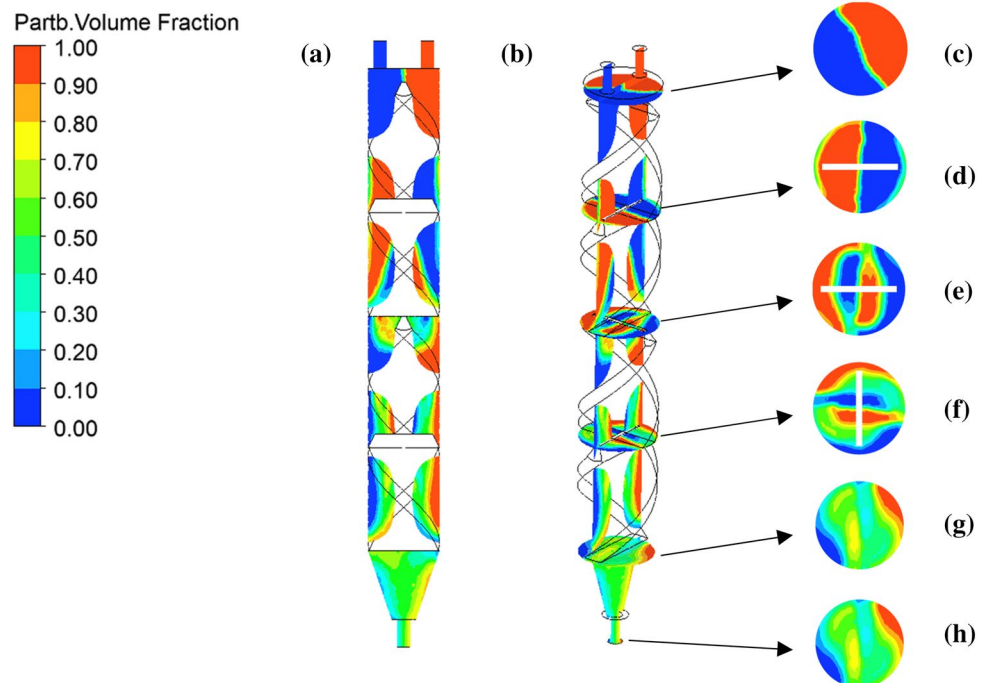




**Fig. 9** VoF modeling of *Part B* resin in ND1M. **a** Axial view at the center, **b** isometric view with cross-sectional views before and after each mixing element, **c–g** zoomed-in cross-sectional views for each shown in **b**, **g** at the outlet

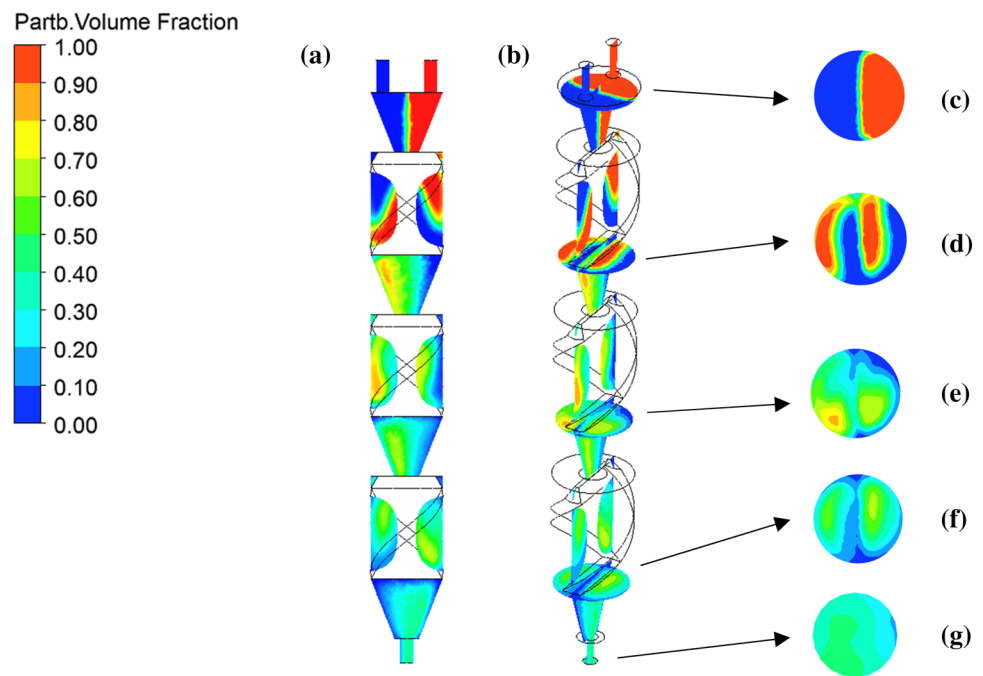
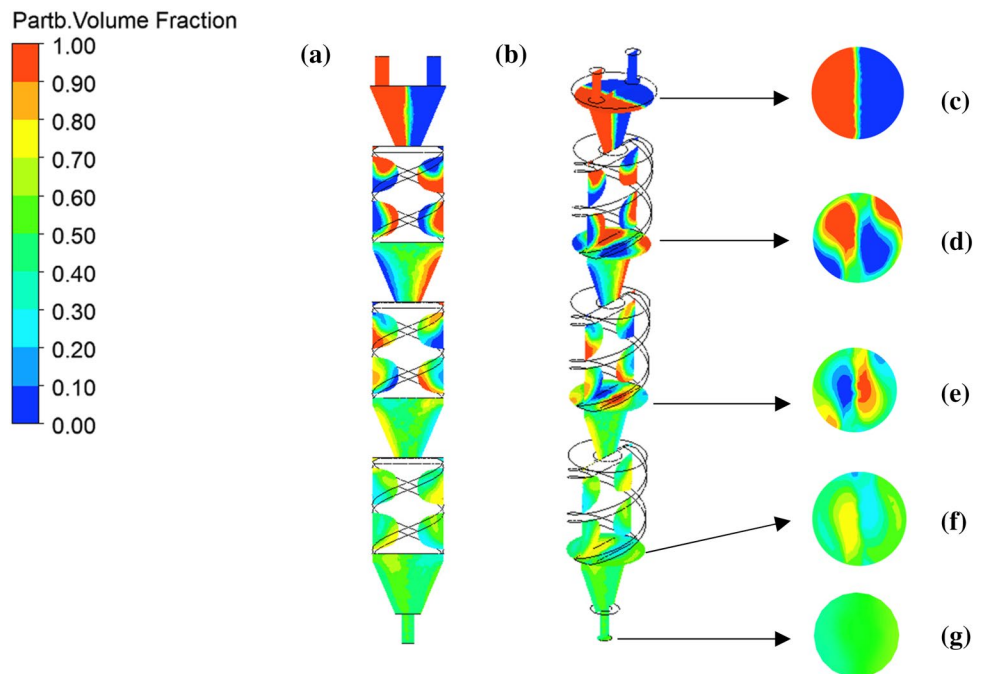


**Fig. 10** VoF modeling of *Part B* resin in ND2M. **a** Axial view at the center, **b** isometric view with cross-sectional views before and after each mixing element, **c–g** zoomed-in cross-sectional views for each shown in **b**, **g** at the outlet



observation of the preliminary tests using the KSM design where the ridge of printed paths remained tacky and could not support the upper layers. In general, commercially available static mixers such as KSM, Komax, and SMX poorly mix liquids in a slow flow regime (e.g.,  $Re < 40$ ) [45], let alone for such an extremely slow flow rate ( $Re = 3.87 \times 10^{-5}$ ) in this study.

The ND1M mixed the components more effectively compared to the KSM, as illustrated in Fig. 9. This improvement

is due to the incorporation of funnel-shaped channels before the mixing elements. The funnels contribute to a better mixing performance in two ways: i) the conical shape prompts the dispersion before the mixture is split into two by the helical blades, and ii) the small orifice size (4 mm diameter) increases the  $\Delta p$  across the mixer. The power consumption to pump the resins into a mixer is directly proportional to the  $\Delta p$ , thus the ideal static mixer actually achieves efficient mixing at a low  $\Delta p$  [45]. However, in the case of an

extremely slow flow regime, the intrinsic low-pressure gradient is inadequate to generate the required mixing shear. The  $\Delta p$  (1.31 MPa) in ND1M is  $\sim 138\%$  higher than the calculated  $\Delta p$  in KSM indicating a higher mixing shear in ND1M. The effects of using the funnel channels on the dispersion of the components are captured in VF contour of ND1M. Figure 9a shows that the green regions representing  $VF \approx 0.5$  at the upstream regions are substantially larger compared to the VF contour of KSM shown in Fig. 8a. Moreover, Fig. 9b shows that the growth rate of the green regions is higher across ND1M compared to KSM (Fig. 8b). However, a patchy dispersion still presented frequently across ND1M. Some trace of *Part A* presented at the outlet of ND1M (Fig. 9h) demonstrates that the distributive mixing of the resins was inadequate to produce a homogenous network.

The mixing element of ND2M has a higher contact surface as the rectangular profile rotated  $360^\circ$  (Fig. 1c) compared to  $180^\circ$  for ND1M (Fig. 1b) along the same length. The increase in the contact angle of ND2M blades caused a greater  $\Delta p$  ( $= 2.82$  MPa) in contrast to 1.31 MPa in ND1M. The influence of changes in the blade design on the mixing performance is noticeable by comparing the VF contour of ND1M (Fig. 9d) and ND2M (Fig. 10d) after the first mixing element. Further analysis of the VF contours at the cross-sections revealed that the green regions ( $\approx VF = 0.5$ ) are more dominant across ND2M (Fig. 10c–g) compared to ND1M (Fig. 9c–g). Figure 10g shows the distributive mixing of ND2M was improved compared with ND1M (Fig. 9g) and a homogenous mixture was achieved at the outlet. These results support the assumption that a higher  $\Delta p$  and contact surface are favorable for efficient mixing performance in extremely slow flow regimes.

The homogeneity of the mixtures was quantified by means of calculating the CoV from Eq. (4) at multiple cross-sections over the length of the mixers. The first cross-section was defined before the first mixing element (axial position = 0) followed by creating 89 cross-sections equally

spaced downstream. Figure 11 shows CoV values of concentrations along the axial position of the mixers. CoV is standard deviation of concentration over the mean concentration of  $n$  data points, thus  $CoV = 0$  represents a complete distributive mixing. However, the homogeneity of a solution is considered satisfactory once the CoV value is less than 0.05 [45]. The analysis of calculated CoV in mixers clearly shows the mixing performance of ND2M is superior compared to KSM, and ND1M. The ND2M achieved  $CoV = 0.02$  while the lowest COV values of KSM, and ND1M were 0.25 and 0.13, respectively. Hence, it is concluded that the ND2M is capable of mixing the resins homogeneously and it is chosen for further optimization of the printing parameters.

## 3.2 Experimental results

### 3.2.1 3D printing of the static mixer

The SLA printed with 405 nm UV-sensitive resin was used to 3D print the ND2M. The model was exported into a slicer software, and the parameters shown in Table 3 were defined for the printing. The printed mixer was washed with Isopropyl alcohol 100% to clean and dissolve uncured resin. The printed model (Fig. 12) is exposed to intense UV light for 20 min to complete the curing process.

### 3.2.2 Optimized printing parameters

Multiple combinations of  $Q$ ,  $V$  sought to identify the optimum printing parameters. The convective heater is used to

**Fig. 11** Comparison of CoV values along the axial position in the static mixers

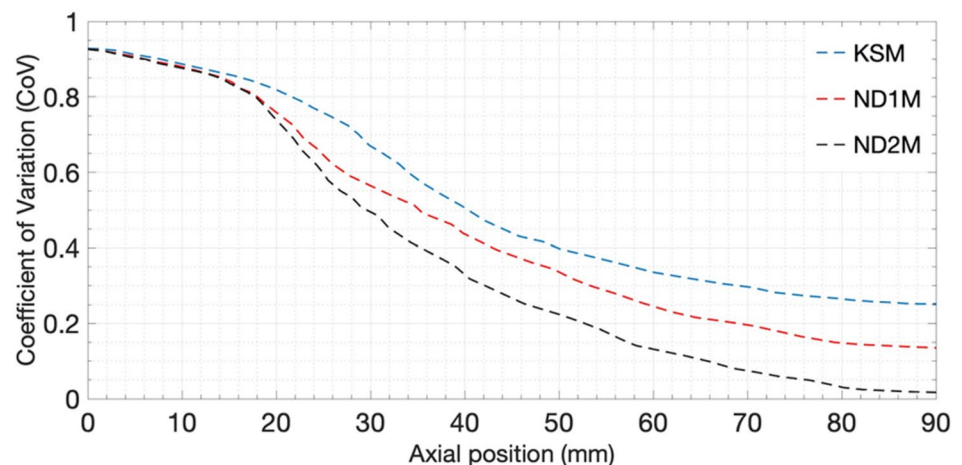


**Table 3** The 3D printing parameters for fabrication of the mixers

Layer thickness (mm)	Normal exposure time (s)	Off time (s)	Bottom exposure time (s)	Bottom layers
0.05	5	0.05	80	3

**Fig. 12** An image of the 3D-printed ND2M

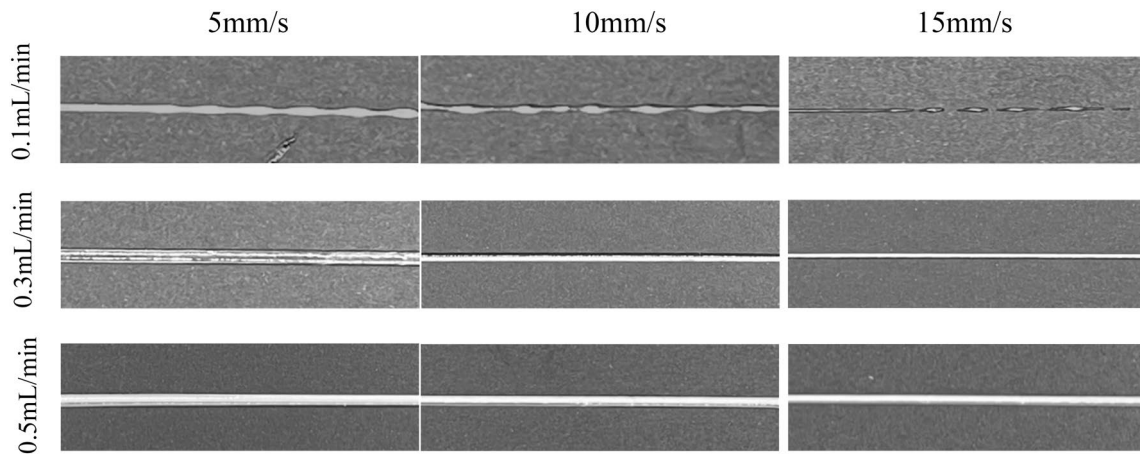


**Fig. 13** Images of printed samples for evaluating the printing parameters; nozzle speed from left to right 5, 10, and 15 mm/s, and flow rate of 0.1, 0.3, and 0.5 mL/min, from top to bottom, respectively

**Table 4** Experimental values of the printed strand diameter  $D_s$

Flow rate, $Q$ (mL/min)	Print speed, $V$		
	5 mm/s	10 mm/s	15 mm/s
0.1	0.82 mm	0.58 mm	0.47 mm
0.3	1.42 mm	1.01 mm	0.82 mm
0.5	1.84 mm	1.30 mm	1.06 mm

**Table 5** Optimum printing parameters

Flow rate (mL/min)	Print speed (mm/s)	Layer width (mm)	Layer height (mm)	Infill density (%)	Infill pattern
0.3	10	1	1	100	Line 45°

shorten the curing time of the silicone to avoid self-collapsing of the parts. A heating temperature of 80 °C showed an adequate acceleration of the curing process so that underlying layers could support the weight of subsequent layers. Nine sets of experiments as described in Sect. 2.4 were performed. Figure 13 shows the images of the printed fibers where three different shapes of fibers, namely discontinuous, straight, and curved were observed.

As shown in Fig. 13, discontinuous fibers are printed at all 3D print speeds with a 0.1 mL/min flow rate. The quality of 3D-printed fibers was acceptable for 0.3, and 0.5 mL/min flow rates. The extruded ink  $D_e$ , (see Fig. 3) was measured as 1 mm immediately after the nozzle tip. However, the diameter of the deposited fiber (i.e., strand diameter  $D_s$ ) is a function of both flow rate  $Q$ , and print speed  $V$ . The

measurement of  $D_s$  for various combinations of  $Q$ ,  $V$  (see Table 4) showed  $D_s$  diameter is directly proportional to  $Q$ , and inversely proportional to  $V$ , where  $D_s$  widened as  $Q$  increased and narrowed by increases of  $V$ . The combination of  $Q$ : 0.3 mL/min, and  $V$ : 10 mm/s resulted  $D_s = 1.01$  mm which has the smallest deviation from  $D_e = 1$  mm. Thus, this combination was used to determine the optimum printing layer height. 5 layers of fibers with a length of 100 mm were printed to create a wall with a thickness of 1 mm. The layer height parameter varied between 0.5 mm to 1.25 mm with 0.25 mm intervals. In which, the layer height parameter set as 1 mm showed acceptable print quality. The optimum values of the printing parameters determined in this study are summarized in Table 5.

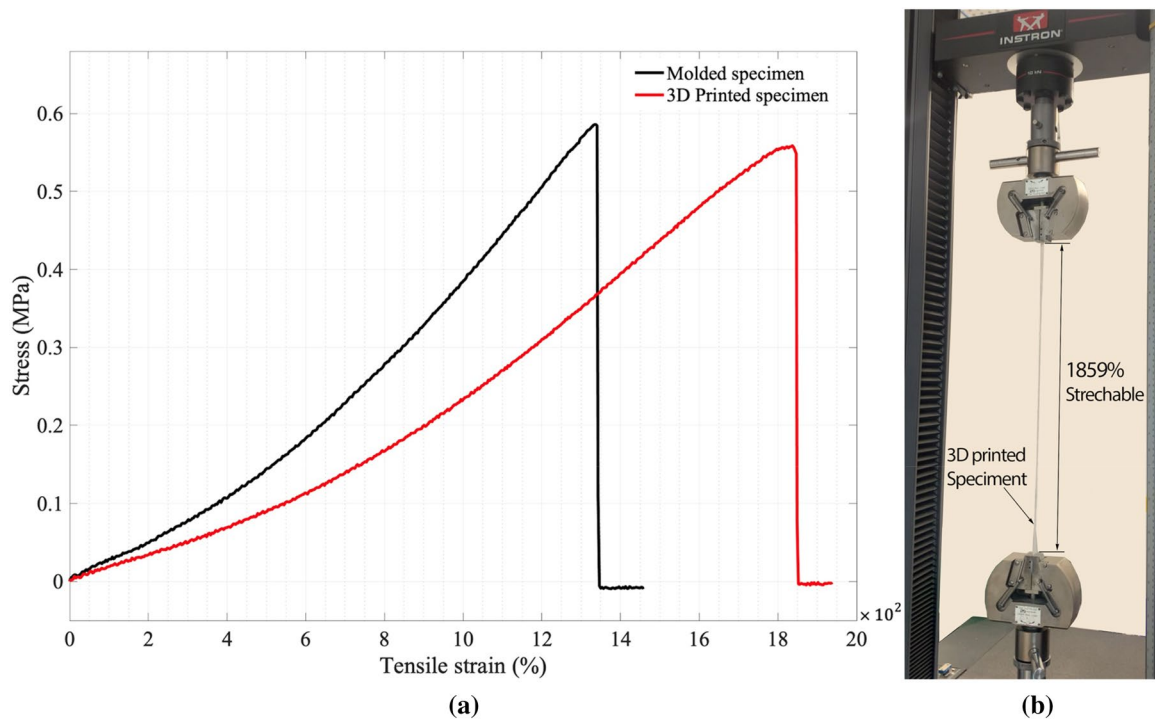


**Fig. 14** Measurements of mechanical properties. **a** Tensile measurement comparing a molded and 3D-printed sample. **b** Image of 3D-printed sample in the tensile testing machine

### 3.2.3 Mechanical properties of molded and 3D-printed silicones

The structural behavior of the 3D-printed and molded samples were analyzed based on the results of the tensile tests. The stress–strain curves of the samples (e.g., Fig. 14a) were plotted to determine the mechanical properties including ultimate tensile stress, elongation at break, and Young’s modulus. The Young’s modulus for each sample was calculated at 100% strain due to the high stretchability of soft silicone [46]. The 3D-printed samples were able to

stretch  $\sim 1859\%$  of their initial length (see Fig. 14b) compared to  $\sim 1346\%$  for molded samples (i.e.,  $\sim 38\%$  more elongation). The required force to stretch a 3D-printed sample from its initial length of 33 mm to its breaking length ( $\sim 613$  mm) was measured to be 12.18 N, demonstrating high stretchability, and a low elastic modulus of the 3D-printed sample. The ultimate tensile strength for the printed and molded samples was comparable (Fig. 15a). However, the calculated Young’s modulus of the printed samples was lower than molded counterparts (see Table 6). This change

**Fig. 15** A comparison of mechanical properties for both molded and 3D-printed specimens, **a** ultimate tensile strength, **b** Young’s modulus, **c** stretchability

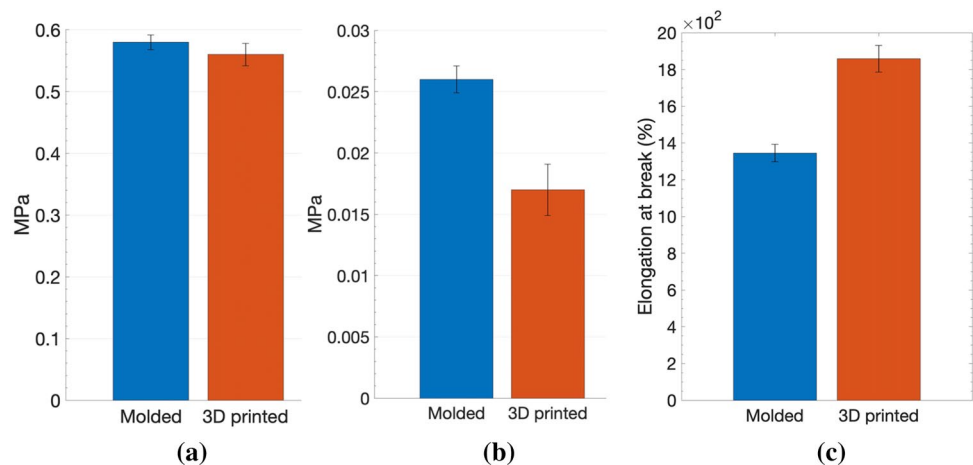


**Fig. 16** Demonstration of the extrusion system application in soft robotics. **a** 3D printing of the soft actuator, **b** 3D-printed soft actuator before actuation, and **c** after actuation

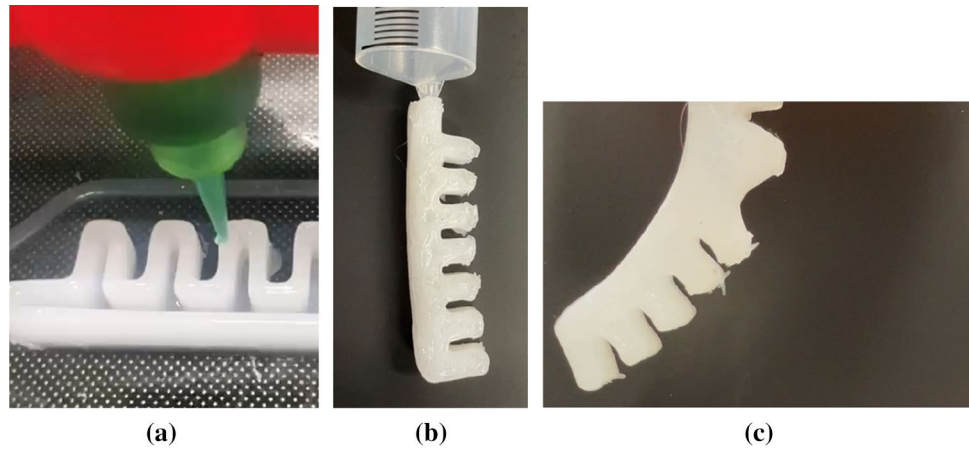


**Table 6** Summary of the average value of mechanical properties for the molded and 3D-printed specimens

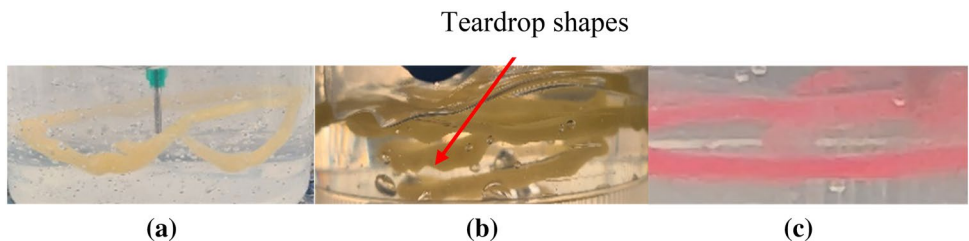
	Young’s modulus (MPa)	Ultimate tensile strength (MPa)	Elongation at break (%)
Molded	0.026	0.58	1346
3D Printed	0.017	0.56	1859

could have resulted from a small increase in the porosity of the 3D-printed samples.

**3.2.4 3D printing of the soft actuator**

The 3D model of the actuator was designed in Fusion 360 as described in Sect. 2.7. The .stl file was exported into a slicer software and the G-code was generated based on the printing parameters described in Table 5. The actuator was printed in 2 min (Fig. 16a) and after 4 h was pulled out to be tested. The side wall was punched with a 0.2 mm biopsy punch and the tip of a 50 mL syringe was inserted to pressurize it (Fig. 16b). The syringe plunger pumped 20 ml of air into the soft actuator causing the model to bend around 45° (Fig. 16c). The gap between the channels (see Fig. 16a) was sealed completely and repetitive tests showed no sign of leakage.

**Fig. 17** Printed samples via FRE method. **a** A low-viscosity gel bath 0.25% w/v carbomer/water. **b** A high-viscosity gel bath 1% w/v carbomer/water. **c** A gel bath with 0.6% w/v carbomer/water



**3.2.5 3D printing of the heart model via FRE method**

Once the optimum printing parameters were determined, the same gantry system was used to print silicone in a gel bath without a heater. The initial printing tests with various viscosities indicated that the printing quality is highly sensitive to the viscosity of the gel bath. The printed samples failed in the gel bath with a lower viscosity (see Fig. 17a) due to inadequate support. In a gel bath with a higher viscosity than EcoFlex’s viscosity, teardrop shapes were developed (see Fig. 17b) as the excessive drag force smudged the extruded silicone.

Various gel bath samples were prepared to match the viscosity of the gel bath with EcoFlex’s viscosity. The results (see Fig. 18) showed that the viscosity of the gel

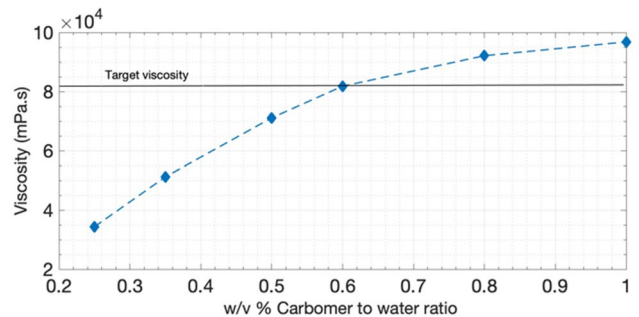
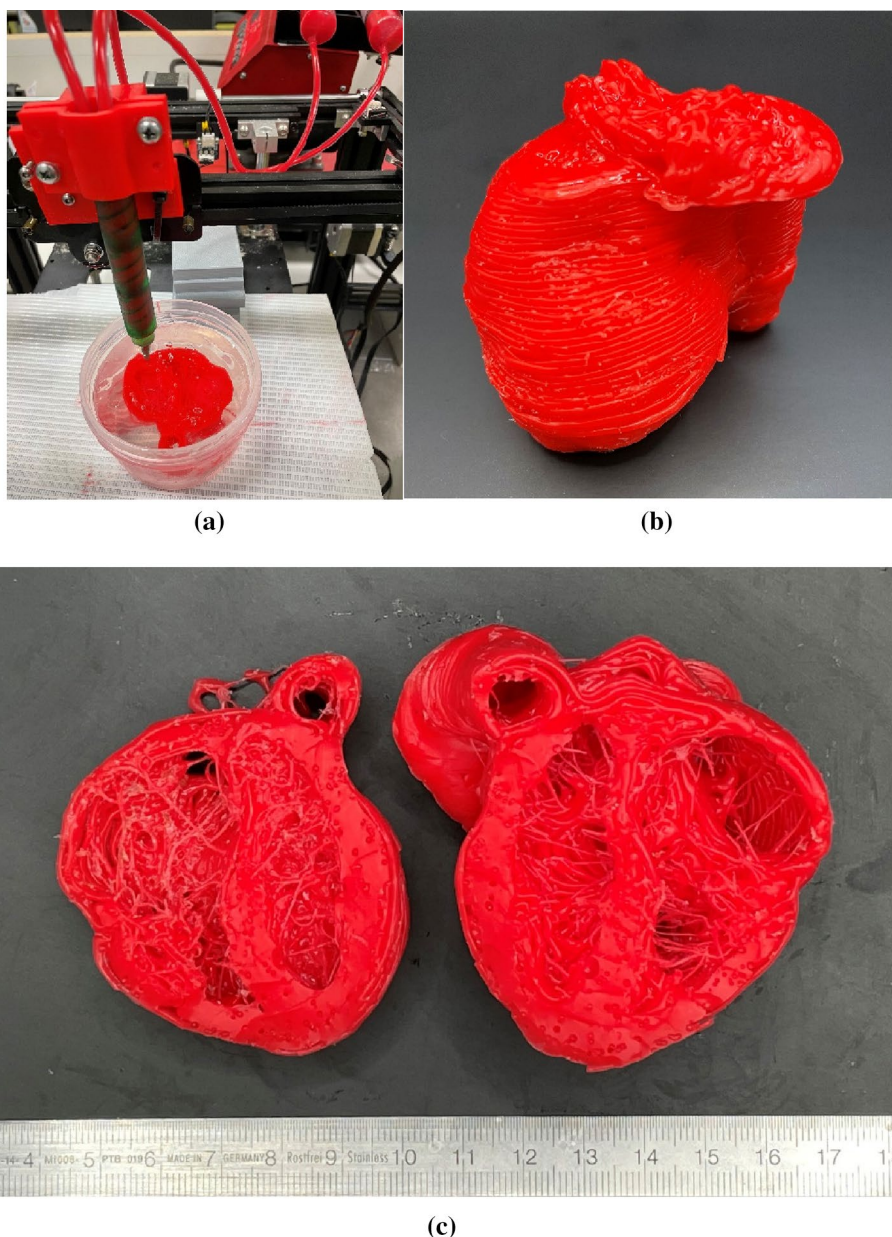


**Fig. 18** PAA gel bath’s viscosity for various carbomer/water ratios

**Fig. 19** **a** Printing setup, **b** outer surface of the 3D-printed heart showing the overhanging feature, **c** cross-sectional views of the 3D-printed heart showing the cavities and extrusion residuals



bath with 0.6% w/v carbomer to water has similar viscosity (i.e., 81580 mPa.s) to EcoFlex with 4% v/v THIVEX. It is observed that printed spiral features formed uniform fibers in the 0.6% w/v carbomer to water gel bath (see Fig. 17c). This finding also supports the assumption of the gel bath's viscosity needs to be matched with the viscosity of the extruded silicone.

To demonstrate the potential of the application of the developed extrusion system in medical training, a heart model shown in Fig. 6 with hollow chambers and overhanging features were fabricated. The model was printed in a gel bath with 0.6% w/v carbomer/water using printing parameters described in Table 5. The printing process was completed after 1 h and 11 min, the part was retrieved

from the gel bath after 4 h and washed with water to clear the gel bath residuals. Overall, the results showed that such a complex design with overhanging features (see Fig. 19b) and internal cavities could be printed which is not possible without using the FRE approach. However, quantitative analysis was out of the scope of this study, and deviations between the 3D models and the printed counterparts were not evaluated. The quality of the printed heart model was inferior compared to the printed soft actuator. Moreover, some silicone fibers were deposited in the space within the ridges of the heart muscles (Fig. 19c) which are intended to be clear cavities as depicted in Fig. 6b–c. There are multiple factors that possibly contributed to the low quality of the print. In this study, the outside diameter (OD) of the

suspended mixer and nozzle tip in the gel bath were 16 mm and 1 mm, respectively. The occupied space by the mixer was significantly larger than a suspended needle, with ODs ranging from 0.1 to 0.4 mm used in other FRE studies [43, 47]. The movement of the (bulky) mixer could have disturbed the deposited layers and adversely affected the print quality. In addition, silicone resins were continuously injected into the mixer leading to unwanted depositions of silicone fibers in the cavities while the nozzle was traveling.

## 4 Discussion

In general, 3D printing of LSRs is extremely challenging and requires a particular method to process the liquid silicone into a 3D structure. One-part resins or moisture-cured silicone fields [48] are prone to moisture contamination and premature curing. The curing time is prolonged and often parts have uneven degrees of curing due to internal layers being exposed to less moisture. Two-part resins need meticulously even mixing, which was previously achieved using an active mixer [32] or a static mixer in a low-viscosity mixture (~1500 mPa.s) [33]. The active mixer could handle a higher viscosity (~23000 mPa.s); however, the mixer had five individual parts which must be assembled leakage free under pumping pressure which required a precise fabrication method. The active mixer causes instability to the system and printing quality due to its vibrations which needed to be managed. In addition, its ability to mix high-viscosity resins is yet to be shown. Higher viscosity resins (e.g., EcoFlex 00-50) have longer polymer chains and are more stretchable compared to their counterparts (e.g., Dragon skin™, Ecoflex 00-30). The static mixer (ND2M) developed in this study could evenly mix a highly viscous resin (~81000 mPa.s). In this study, the elongation at break of the 3D-printed samples was measured at ~1850%, which is higher than other works that reported up to ~1500% [9, 15], demonstrating the capability of the developed system to print highly stretchable structures. This capability enhances the current progress in the development of 3D structured stretchable sensors [49], for example, in haptic applications. Furthermore, injected resins into the static mixer were effectively washed out without apparent flow stagnation. This is an important aspect of the developed mixer as the residuals will be cured inside the mixer causing blockage and would disturb the printing process, leading to poor print quality, similar to those observed in Morrow et al.'s study [31]. The print resolution of 1 mm is achieved in this study, and a pneumatic actuator with a wall thickness of 1 mm was printed. The printed actuator's shape was close to the modeled actuator except for small spike shape residuals on the outer surfaces. The 1 mm gap between the walls was successfully closed and the printed silicone formed a nearly flat roof and the side

walls. The inflated actuator could bend (see Fig. 16c) without air leakage, assuring the extrusion system can be used to fabricate soft actuators. However, the first chamber actuated more than the other chambers indicating the design should be further tuned in the future to achieve a higher bending angle with uniform actuation.

Silicone-based tissue mimicking phantoms has significant applications in the medical training [50]. It is extremely challenging to fabricate a realistic model with conventional methods (e.g., molding), particularly in a patient-specific manner from medical imaging. Commercial 3D printing technologies, such as PolyJet from Stratatsys can directly 3D print soft models, but these elastomeric materials have limited strains and robustness, especially in wet environments. 3D printing of silicone phantoms was not possible due to the intrinsically difficult printing process and relatively short printing time associated with most of the previously developed extrusion systems. The developed mixer can print for a prolonged period and could be used to fabricate tissue mimicking phantoms with a complex shape, such as the printed heart model (see Fig. 19). The challenging features, such as the internal cavities and overhanging features were fabricated. However, some unwanted silicone fibers did remain in the voids (See Fig. 19c). These artifacts are due to the continuous extrusion of silicone from the nozzle while the nozzle is traveling. Further development is required to effectively control the flow rate while the nozzle is traveling. The ND2M mixer showed that it could evenly mix the two-part resin with a relatively low-pressure drop of  $\approx 3$  MPa, eliminating the need to incorporate an expensive high-torque pumping system [32] or a multi-pumping system [33]. The developed extrusion system is cost-effective where the total cost was less than \$2000AUD (see Table 2).

## 5 Conclusion

This work successfully presented a cost-effective approach for 3D printing of a two-part silicone resin to fabricate highly stretchable structures. The printing parameters were determined empirically and can be used in an open-source slicer software to generate a G-code for a 3D printer. The mechanical properties of the printed samples were compared to their molded counterpart. It is shown that the 3D-printed sample was able to stretch 38% more than the molded one before it broke at an elongation of 1859%. The application of highly stretchable and soft silicone products as soft actuators was demonstrated. The potential of the proposed method for 3D printing more complex structures with internal voids such as the human heart was also presented. This study shows promising outcomes for future 3D printing of soft materials utilizing the DIW technique in applications such

as medical prosthetics, flexible electronics, soft robotics, and medical training.

**Funding** Open Access funding enabled and organized by CAUL and its Member Institutions.

## Declarations

**Conflict of interest** The authors did not receive support from any organization for the submitted work. The authors have no relevant financial or non-financial interests to disclose.

**Open Access** This article is licensed under a Creative Commons Attribution 4.0 International License, which permits use, sharing, adaptation, distribution and reproduction in any medium or format, as long as you give appropriate credit to the original author(s) and the source, provide a link to the Creative Commons licence, and indicate if changes were made. The images or other third party material in this article are included in the article's Creative Commons licence, unless indicated otherwise in a credit line to the material. If material is not included in the article's Creative Commons licence and your intended use is not permitted by statutory regulation or exceeds the permitted use, you will need to obtain permission directly from the copyright holder. To view a copy of this licence, visit <http://creativecommons.org/licenses/by/4.0/>.

## References

- Zhalmuratova D, Chung H-J (2020) Reinforced gels and elastomers for biomedical and soft robotics applications. *ACS Appl Polym Mater* 2(3):1073–1091
- Zare M et al (2021) Silicone-based biomaterials for biomedical applications: antimicrobial strategies and 3D printing technologies. *J Appl Polym Sci* 138(38):50969
- Sparrman B et al (2021) Printed silicone pneumatic actuators for soft robotics. *Addit Manuf* 40:101860
- Zolfagharian A et al (2022) Silicon-based soft parallel robots 4D printing and multiphysics analysis. *Smart Mater Struct* 31:1150
- Kalkal A et al (2021) Recent advances in 3D printing technologies for wearable (bio)sensors. *Addit Manuf* 46:102088
- Fortunato GM et al (2022) Surface reconstruction and tissue recognition for robotic-based in situ bioprinting. *Bioprinting* 26:e00195
- Tyagi M, Pan J, Jager EW (2019) Novel fabrication of soft microactuators with morphological computing using soft lithography. *Microsyst Nanoeng* 5(1):1–10
- Li J et al (2022) 3D printing of silicone elastomers for soft actuators. *Actuators* 11:200
- Herzberger J et al (2019) Polymer design for 3D printing elastomers: recent advances in structure, properties, and printing. *Prog Polym Sci* 97:101144
- Liravi F, Toyserkani E (2018) Additive manufacturing of silicone structures: a review and prospective. *Addit Manuf* 24:232–242
- Femmer T, Kuehne AJC, Wessling M (2014) Print your own membrane: direct rapid prototyping of polydimethylsiloxane. *Lab Chip* 14(15):2610–2613
- Bhattacharjee N et al (2018) Desktop-stereolithography 3D-printing of a poly(dimethylsiloxane)-based Material with sylgard-184 properties. *Adv Mater* 30(22):1800001
- Kim DS, Tai BL (2016) Hydrostatic support-free fabrication of three-dimensional soft structures. *J Manuf Process* 24:391–396
- Al Rashid A et al (2021) Vat photopolymerization of polymers and polymer composites: processes and applications. *Addit Manuf* 47:102279
- Jiang B et al (2022) Recent advances in UV/thermal curing silicone polymers. *Chem Eng J* 435:134843
- Kim DS et al (2019) Feasibility study of silicone stereolithography with an optically created dead zone. *Addit Manuf* 29:100793
- Liravi F et al (2019) High-speed material jetting additive manufacturing of silicone structures: mechanical characterization. *Progress Addit Manuf* 4(4):479–495
- McCoul D et al (2017) Inkjet 3D printing of UV and thermal cure silicone elastomers for dielectric elastomer actuators. *Smart Mater Struct* 26(12):125022
- Liravi F, Toyserkani E (2018) A hybrid additive manufacturing method for the fabrication of silicone bio-structures: 3D printing optimization and surface characterization. *Mater Des* 138:46–61
- Yang H et al (2013) High viscosity jetting system for 3D reactive inkjet printing. In 2013 International Solid Freeform Fabrication Symposium. University of Texas at Austin.
- Selbertinger E, Achenbach F, Pachaly B (2019) Method for producing silicone elastomer parts. Google Patents
- Guo Y et al (2017) Inkjet and inkjet-based 3D printing: connecting fluid properties and printing performance. *Rapid Prototyp J* 23(3):562–576
- Hinton TJ et al (2016) 3D printing PDMS elastomer in a hydrophilic support bath via freeform reversible embedding. *ACS Biomater Sci Eng* 2(10):1781–1786
- O'Bryan Christopher S, Tapomoy Bhattacharjee, Samuel Hart, Kabb Christopher P, Schulze Kyle D, Indrasena Chilakala, Sumerlin Brent S, Gregory Sawyer W, Angelini Thomas E et al (2017) Self-assembled micro-organogels for 3D printing silicone structures. *Sci Adv* 3(5):e1602800
- Shah PP et al (2020) Extrusion-based 3D bioprinting of alginate-based tissue constructs. *Procedia CIRP* 95:143–148
- Armstrong AA et al (2021) Process monitoring and control strategies in extrusion-based bioprinting to fabricate spatially graded structures. *Bioprinting* 21:e00126
- Allencherry J et al (2022) Investigation of Hydrogel and gelatin bath formulations for extrusion-based 3D bioprinting using deep learning. *Procedia CIRP* 110:360–365
- Davoodi E et al (2020) Extrusion and microfluidic-based bioprinting to fabricate biomimetic tissues and organs. *Adv Mater Technol* 5(8):1901044
- Kuthe S et al (2022) 3D printed mechanically representative aortic model made of gelatin fiber reinforced silicone composite. *Mater Lett* 320:132396
- Woo R et al (2021) Structure-mechanical property relationships of 3D-printed porous polydimethylsiloxane. *ACS Appl Polym Mater* 3(7):3496–3503
- Morrow J, Hemleben S, Menguc Y (2017) Directly fabricating soft robotic actuators with an open-source 3-D printer. *IEEE Robot Autom Lett* 2(1):277–281
- Yirmibesoglu OD et al (2018) Direct 3D printing of silicone elastomer soft robots and their performance comparison with molded counterparts. In: 2018 IEEE international conference on soft robotics (RoboSoft)
- Miriyev A et al (2019) Additive manufacturing of silicone composites for soft actuation. *3D Print Addit Manuf* 6(6):309–318
- ANSYS. *Fluent theory guide, Release 15*. 2013 [cited 2022 17/06]; Available from: <https://www.afs.enea.it/project/neptunius/docs/fluent/html/th/node299.htm>.
- Pianko-Oprych P, Jaworski Z (2009) CFD modelling of two-phase liquid-liquid flow in a SMX static mixer. *Pol J Chem Technol* 11(3):41–49



36. Zhai S, Song L, Lv X (2019) Measurement and analysis of silicone oil characteristics and viscositytemperature index. IOP conference series earth and environmental science. IOP, Bristol
37. Liang J (2008) Effects of extrusion conditions on die-swell behavior of polypropylene/diatomite composite melts. *Polym Test* 27(8):936–940
38. Smith PT et al (2018) Chemical modification and printability of shear-thinning hydrogel inks for direct-write 3D printing. *Polymer* 152:42–50
39. Sharma A (2013) Finding Biodegradable alternatives for Petroleum-based polymers. *Rice Undergraduate Sci Res* 6:23–36
40. Calais T et al (2022) Mechanical characterization of 3D-printed silicone/epoxy hybrids. *Mater Today: Proc* 70:218–223
41. Anand Kumar S, Shivraj Narayan Y (2019) (2019) Tensile testing and evaluation of 3D-printed PLA specimens as per ASTM D638 type IV standard. Innovative design, analysis and development practices in aerospace and automotive engineering (I-DAD 2018). Springer, Singapore, pp 79–95
42. ASTM International; West Conshohocken, P., USA. *Standard Test Methods for Vulcanized Rubber and Thermoplastic Elastomers—Tension*. [cited 2022 13 October]; Available from: <https://www.astm.org/d0412-16.html>.
43. Lee A et al (2019) 3D bioprinting of collagen to rebuild components of the human heart. *Science* 365(6452):482–487
44. Sakai T (2014) Experimental verification of homogeneity in polymer gels. *Polym J* 46(9):517–523
45. Haddadi MM et al (2020) Comparative analysis of different static mixers performance by CFD technique: an innovative mixer. *Chin J Chem Eng* 28(3):672–684
46. Feng L, Li S, Feng S (2017) Preparation and characterization of silicone rubber with high modulus via tension spring-type crosslinking. *RSC Adv* 7(22):13130–13137
47. Menon A et al (2019) Optimization of silicone 3D printing with hierarchical machine learning. *3D Print Addit Manuf.* 6(4):181–189
48. Plott J, Shih A (2017) The extrusion-based additive manufacturing of moisture-cured silicone elastomer with minimal void for pneumatic actuators. *Addit Manuf* 17:1–14
49. Luis E et al (2018) A review of medical silicone 3d printing technologies and clinical applications. *J Orthop Ther: JORT*. <https://doi.org/10.29011/2575-8241>
50. McGarry CK et al (2020) Tissue mimicking materials for imaging and therapy phantoms: a review. *Phys Med Biol*. <https://doi.org/10.1088/1361-6560/abbd17>

**Publisher's Note** Springer Nature remains neutral with regard to jurisdictional claims in published maps and institutional affiliations.